Cell Systems, Volume *14*

Supplemental information

Deciphering tumor ecosystems at super resolution from spatial transcriptomics with TESLA

Jian Hu, Kyle Coleman, Daiwei Zhang, Edward B. Lee, Humam Kadara, Linghua Wang, and Mingyao Li

Supplemental information

Deciphering tumor ecosystems at super-resolution from spatial transcriptomics with TESLA

Jian Hu, Kyle Coleman, Daiwei Zhang, Humam Kadara, Edward B. Lee, Linghua Wang, Mingyao Li

Table S1. Datasets analyzed in this paper.

Species	Tissue	Data source	Dataset dimensions	Protocol	Spot diameter by pixels
Human	Invasive ductal carcinoma	10x Genomics (https://support.10xgenomics.com/spatial-gene-expression/datasets/1.2.0/V1_Human_Invasive_Ductal_Carcinoma)	4,727 spots 36,601 genes	10x Visium	172 pixels
Human	Cutaneous squamous cell carcinoma	Ji *et al*. GSE144240	646 spots 17,344 genes	10x Visium	200 pixels
Human	Cutaneous squamous cell carcinoma	Ji *et al*. GSE144240	6,824 cells 32,738 genes	10X Chromium 3' v2	NA
Human	Cutaneous malignant melanoma	Thrane *et al*. (https://www.spatialresearch.org/resources-published-datasets/doi-10-1158-0008-5472-can-18-0747/)	293 spots 16,148 genes	Spatial Transcriptomics	350 pixels
Human	Melanoma tumor	Tirosh *et al*. (https://science.sciencemag.org/content/352/6282/189) GSE72056	4,139 cells 23,686 genes	Smart-Seq2	NA

Human	HER2+, ER+ and PR- breast cancer	10x Genomics (https://support.10xgenomics.com/spatial-gene-expression/datasets/1.1.0/V1_Breast_Cancer_Block_A_Section_1)	3,798 spots 36,601 genes	10x Visium	172 pixels
Human	HER2+ breast tumor	Andersson *et al*. (https://github.com/almaan/her2st)	295 spots 15,109 genes	Spatial Transcriptomics	146 pixels
Mouse	Posterior brain (sagittal)	10x Genomics (https://support.10xgenomics.com/spatial-gene-expression/datasets/)	3,355 spots 32,285 genes	10x Visium	80 pixels
Mouse	Kidney (coronal)	10x Genomics (https://support.10xgenomics.com/spatial-gene-expression/datasets/)	1,438 spots 32,285 genes	10x Visium	80 pixels
Human	Clear cell renal cell carcinoma primary tumors	Meylan *et al*. GSE175540	4,359 spots 36,945 genes	10x Visium	24 pixels
Human	Breast cancer	10X Genomics (https://www.10xgenomics.com/products/xenium-in-situ/preview-dataset-human-breast)	167,782 cells, 313 genes	10x Xenium	NA

Table S2. Overlaps with curated gene sets included in the Molecular Signature Database by performing gene set enrichment analysis using region-specific DEGs in the cutaneous squamous carcinoma dataset.

Tumor core enriched genes, n=300				
Name	Description	n	FDR q-value	Genes
REACTOME_METABOLISM_OF_LIPIDS	Metabolism of lipids	26	2.46e-07	AGPAT3, LPIN3, TAZ, PLD1, PNPLA8, LCLAT1, PISD, PLBD1, PITPNM3, MTM1, PI4K2B, HADH, MMUT, PCCB, MECR, MCAT, DECR2, ELOVL6, ALOX12B, FDXR, TBL1X, MTF1, NFYC, HSD17B1, DHRS7B, MED21
REACTOME_GLYCEROPHOSPHOLIPID_BIOSYNTHESIS	Glycerophospholipid biosynthesis	9	0.000589	AGPAT3, LPIN3, TAZ, PLD1, PNPLA8, LCLAT1, PISD, PLBD1, PITPNM3
REACTOME_PHOSPHOLIPID_METABOLISMREACTOME_PHOSPHOLIPID_METABOLISM	Phospholipid metabolism	11	0.000589	AGPAT3, LPIN3, TAZ, PLD1, PNPLA8, LCLAT1, PISD, PLBD1, PITPNM3, MTM1, PI4K2B
REACTOME_MITOCHONDRIAL_FATTY_ACID_BETA_OXIDATION	Mitochondrial Fatty Acid Beta-Oxidation	5	0.00463	HADH, MMUT, PCCB, MECR, MCATHADH, MMUT, PCCB, MECR, MCAT
REACTOME_VESICLE_MEDIATED_TRANSPORT	Vesicle-mediated transport	18	0.00475	AGPAT3, TUBB4A, KIF23, RAB8A, KIF20B, NBAS, BET1L, SYS1, EPGN, VPS37A, DENND2C, DENND1B, MON1A, EPS15L1, AP1M2, COPS7A, FCHO2, EXOC3
REACTOME_SIGNALING_BY_RETINOIC_ACID	Signaling by Retinoic Acid	5	0.00704	DHRS4, PDHB, PDK2, DHRS3, RDH14
REACTOME_CELL_CYCLE_MITOTIC	Cell Cycle, Mitotic	15	0.00768	LPIN3, TUBB4A, KIF23, RAB8A, LIG1, FEN1, CENPF, SEH1L, ZWINT, DHFR, CDC23, ANAPC15, TFDP2, CKS1B, PPP2R3B
REACTOME_FATTY_ACID_METABOLISM	Fatty acid metabolism	8	0.0155	HADH, MMUT, PCCB, MECR, MCAT, DECR2, ELOVL6, ALOX12B
REACTOME_CELL_CYCLE	Cell Cycle	16	0.0178	LPIN3, TUBB4A, KIF23, RAB8A, LIG1, FEN1, CENPF, SEH1L, ZWINT, DHFR, CDC23, ANAPC15, TFDP2, CKS1B, PPP2R3B, MLH1
REACTOME_METABOLISM_OF_AMINO_ACIDS_AND_DERIVATIVES	Metabolism of amino acids and derivatives	11	0.0248	PDHB, PXMP2, GSTZ1, CKB, ALDH9A1, BBOX1, ALDH4A1, PYCR3, SLC25A10, GPT2, ASPG

Tumor edge enriched genes, n=106				
Name	Description	n	FDR q-value	Genes
REACTOME_INNATE_IMMUNE_SYSTEM	Innate Immune System	18	5.19e-07	PTPN6, C2, FPR1, C3, PTAFR, FCGR1A, LILRB2, LAIR1, PTPRJ, FCER1G, MME, RHOF, BIN2, STK10, FCGR3A, FYN, DUSP4, CLU
HALLMARK_INTERFERON_GAMMA_RESPONSE	Genes up-regulated in response to IFNG GeneID=3458	9	1.8e-06	PTPN6, IL2RB, IRF8, FPR1, FCGR1A, GBP4, ST3GAL5, CMPK2, ZNFX1PTPN6, IL2RB, IRF8, FPR1, FCGR1A, GBP4, ST3GAL5, CMPK2, ZNFX1
REACTOME_NEUTROPHIL_DEGRANULATION	Neutrophil degranulation	12	2.46e-06	PTPN6, FPR1, C3, PTAFR, LILRB2, LAIR1, PTPRJ, FCER1G, MME, RHOF, BIN2, STK10
REACTOME_ADAPTIVE_IMMUNE_SYSTEM	Adaptive Immune System	14	1.23e-05	PTPN6, CD3D, CD3E, FYB1, C3, AKT3, FCGR1A, LILRB2, LAIR1, PTPRJ, FCGR3A, FYN, LILRB4, TRIM39
REACTOME_CYTOKINE_SIGNALING_IN_IMMUNE_SYSTEM	Cytokine Signaling in Immune system	12	0.00011	CCR1, PTPN6, IL2RB, IRF8, FPR1, PTAFR, AKT3, FCGR1A, PTPRJ, FYN, DUSP4, GBP4
KEGG_CHEMOKINE_SIGNALING_PATHWAY	Chemokine signaling pathway	7	0.000156	CCR1, CXCL13, CX3CL1, CCR7, CXCL12, AKT3, CCL18
PID_TCR_PATHWAY	TCR signaling in native CD4+ T cells	5	0.000156	PTPN6, CD3D, CD3E, FYB1, FYN
HALLMARK_INFLAMMATORY_RESPONSE	Genes defining inflammatory response	7	0.000187	IL2RB, FPR1, PTAFR, CX3CL1, CCR7, GPR183, RGS16

Table S3. Overlaps with curated gene sets included in the Molecular Signature Database by performing gene set enrichment analysis using region-specific DEGs in the cutaneous malignant melanoma dataset.

Tumor core enriched genes, n=300				
Name	Description	n	FDR q-value	Genes
REACTOME_SIGNALING_BY_RHO_GTPASES_MIRO_GTPASES_AND_RHOBTB3	Signaling by Rho GTPases, Miro GTPases and RHOBTB3.	23	6.96e-06	STAM, CKAP4, AAAS, H2AC19, PTK2, DOCK7, FNBP1L, ARHGEF12, PLXNA1, BAIAP2, SCRIB, ARHGAP32, STARD8, ALDH3A2, LRRC1, EMD, BAIAP2L1, ANKFY1, PAFAH1B1, DVL3, TRAK2, NF2, CENPT
PID_MET_PATHWAY	Signaling events mediated by Hepatocyte Growth Factor Receptor (c-Met)	8	9.39e-05	RAB5A, PTK2, MET, RANBP10, RANBP9, BCAR1, PXN, EIF4EBP1
REACTOME_SIGNALING_BY_MET	Signaling by MET	8	9.39e-05	STAM, USP8, PTK2, DOCK7, MET, RANBP10, RANBP9, ITGA3
REACTOME_RHO_GTPASE_CYCLE	RHO GTPase cycle	16	0.000132	STAM, CKAP4, AAAS, DOCK7, FNBP1L, ARHGEF12, PLXNA1, BAIAP2, SCRIB, ARHGAP32, STARD8, ALDH3A2, LRRC1, EMD, BAIAP2L1, ANKFY1
REACTOME_SIGNALING_BY_RECEPTOR_TYROSINE_KINASESREACTOME_SIGNALING_BY_RECEPTOR_TYROSINE_KINASES	Signaling by Receptor Tyrosine Kinases	15	0.00158	STAM, USP8, PTK2, DOCK7, BAIAP2, MET, RANBP10, RANBP9, BCAR1, PXN, ITGA3, ATP6V1C1, TRIB3, COL9A3, ID4
REACTOME_MET_ACTIVATES_RAS_SIGNALING	MET activates RAS signaling	3	0.0121	MET, RANBP10, RANBP9
REACTOME_SIGNALING_BY_WNT	Signaling by WNT	10	0.026	H2AC19, USP8, PSME3, AXIN1, SCRIB, DVL3, ASH2L, WLS, LGR4, SOX13

Tumor edge enriched genes, n=155				
Name	Description	n	FDR q-value	Genes
HALLMARK_EPITHELIAL_MESENCHYMAL_TRANSITION	Genes defining epithelial-mesenchymal transition, as in wound healing, fibrosis and metastasis	14	6.66e-11	THY1, CAPG, VCAM1, SDC1, LUM, LOXL1, LOXL2, PCOLCE, FBLN1, BGN, IL32, TGFBI, FSTL1, SFRP4

REACTOME_EXTRACELLULAR_MATRIX_ORGANIZATION	Extracellular matrix organization	15	7.62e-10	ITGAL, MMP9, VCAM1, SDC1, LUM, LOXL1, LOXL2, PCOLCE, FBLN1, BGN, PECAM1, VWF, COL6A1, LTBP2, LAMB2
BIOCARTA_TCYTOTOXIC_PATHWAY	T Cytotoxic Cell Surface Molecules	5	3.36e-07	THY1, ITGAL, CD8A, CD2, CD3E
REACTOME_ADAPTIVE_IMMUNE_SYSTEM	Adaptive Immune System	18	1.43e-06	ITGAL, CD8A, HLA-DOA, CD3E, PRKCB, FYB1, VCAM1, CD22, C3, PLCG2, TAB2, FCGR1B, SLAMF7, LILRB2, LAIR1, BLK, ANAPC2, LAG3
REACTOME_CYTOKINE_SIGNALING_IN_IMMUNE_SYSTEM	Cytokine Signaling in Immune system	16	5.79e-06	MMP9, IL4R, IL2RB, CCL19, IRF8, VCAM1, SDC1, IL32, TAB2, FCGR1B, IL10RA, CEBPD, LGALS9, TNFSF13B, CD27, SAMHD1
REACTOME_IMMUNOREGULATORY_INTERACTIONS_BETWEEN_A_LYMPHOID_AND_A_NON_LYMPHOID_CELL	Immunoregulatory interactions between a Lymphoid and a non-Lymphoid cell	9	1.35e-05	ITGAL, CD8A, CD3E, VCAM1, CD22, C3, SLAMF7, LILRB2, LAIR1
BIOCARTA_THELPER_PATHWAY	T Helper Cell Surface Molecules	4	2.03e-05	THY1, ITGAL, CD2, CD3E
REACTOME_SIGNALING_BY_INTERLEUKINS	Signaling by Interleukins	11	0.000247	MMP9, IL4R, IL2RB, CCL19, VCAM1, SDC1, IL32, TAB2, IL10RA, CEBPD, LGALS9
PID_CD8_TCR_DOWNSTREAM_PATHWAY	Downstream signaling in native CD8+ T cells	5	0.000649	CD8A, CD3E, PRKCB, IL2RB, GZMB
KEGG_CYTOKINE_CYTOKINE_RECEPTOR_INTERACTION	Cytokine-cytokine receptor interaction	8	0.00105	IL4R, IL2RB, CCL19, IL10RA, TNFSF13B, CD27, CCL21, CXCL14
HALLMARK_INTERFERON_GAMMA_RESPONSE	Genes up-regulated in response to IFNG	7	0.00139	IL4R, IL2RB, IRF8, VCAM1, SLAMF7, IL10RA, SAMHD1

Table S4. Marker genes used for cell type, tumor region and protein detection.

Target region	Marker genes
B cell	*CD19, CD79A, CD79B, MS4A1, CD22*
CD8+ T cell	*CD8A, CD8B*
Follicular helper T cells	*CD3E, CD3D, CD3G, CD4, PDCD1, CXCR5*
Dendritic cell	*CD1A, CD1B, CD1E, CLEC10A, CLIC2, WFDC21P*
CXCL13	*CXCL13*
Melanoma	*MITF, CSPG4, MAGEA1, MLANA, TYR, SOX10*
Squamous cell carcinoma	*BUB1B, KIF1C, TOP2A, CD151, MMP10, PTHLH, FEZ1, IL24, KCNMA, INHBA, MAGEA4, NT5E, LAMC2, SLITRK6*
Breast Cancer	*ERBB2, CNN1, CDH1, KRT5, KRT7, KRT14, KRT18, CDNND1, GATA3, FOXA1, PIP, SCGB2A2*
HER2+ tumor subtype	*ERBB2*
ER+ tumor subtype	*ESR1*
PgR+ tumor subtype	*PGR*

Table S5. Software compared with TESLA.

Method	Version	URL
BayesSpace	1.0.0	https://github.com/edward130603/BayesSpace
SpaGCN	1.2.0	https://github.com/jianhuupenn/SpaGCN
RCTD	1.2.0	https://github.com/dmcable/RCTD

Fig. S1. Enhanced gene expression by TESLA can better retain the original expression pattern at the spot level than BayesSpace. We randomly selected 10 genes in which BayesSpace's correlation with the observed spot-level gene expression was less than 0.5.

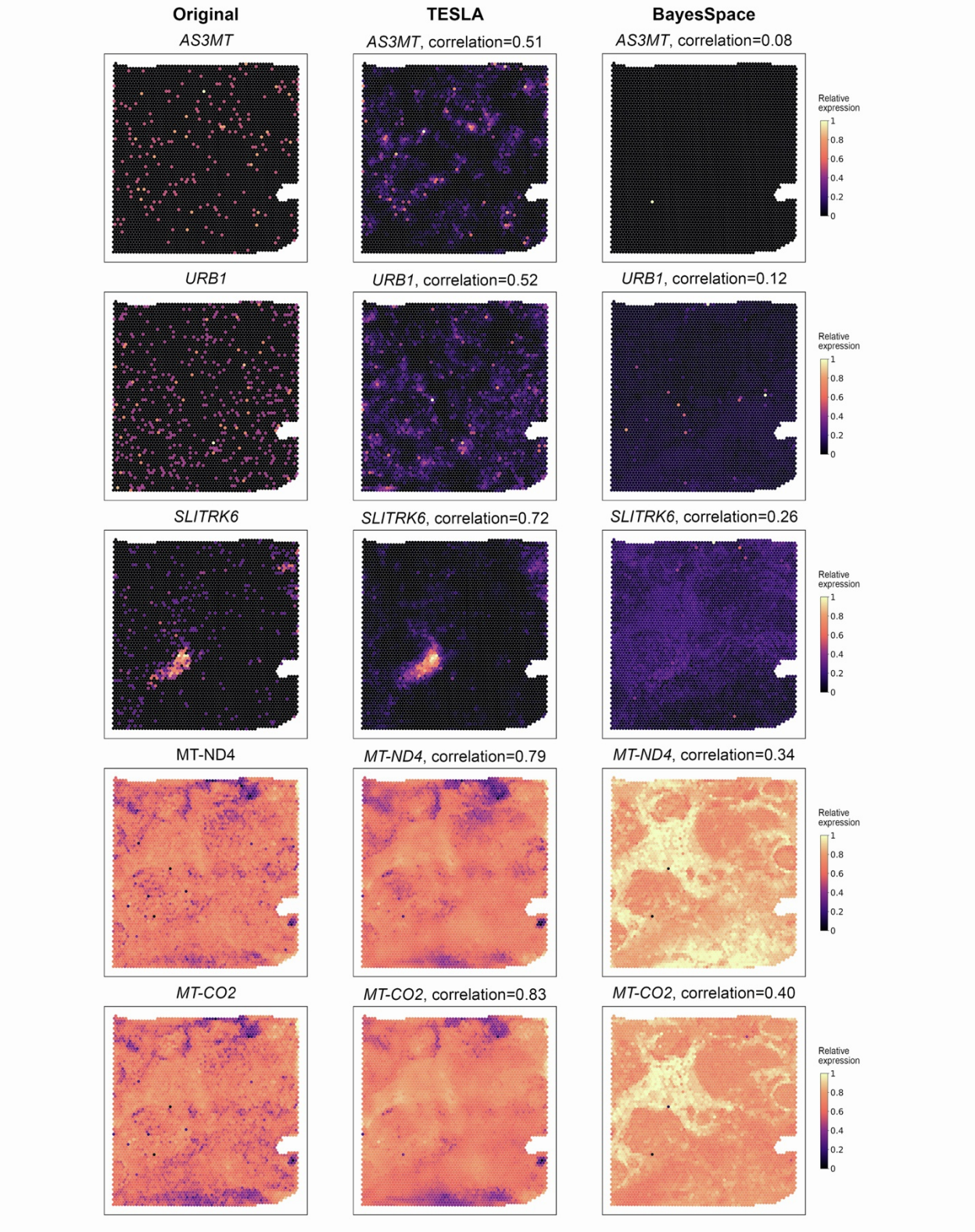

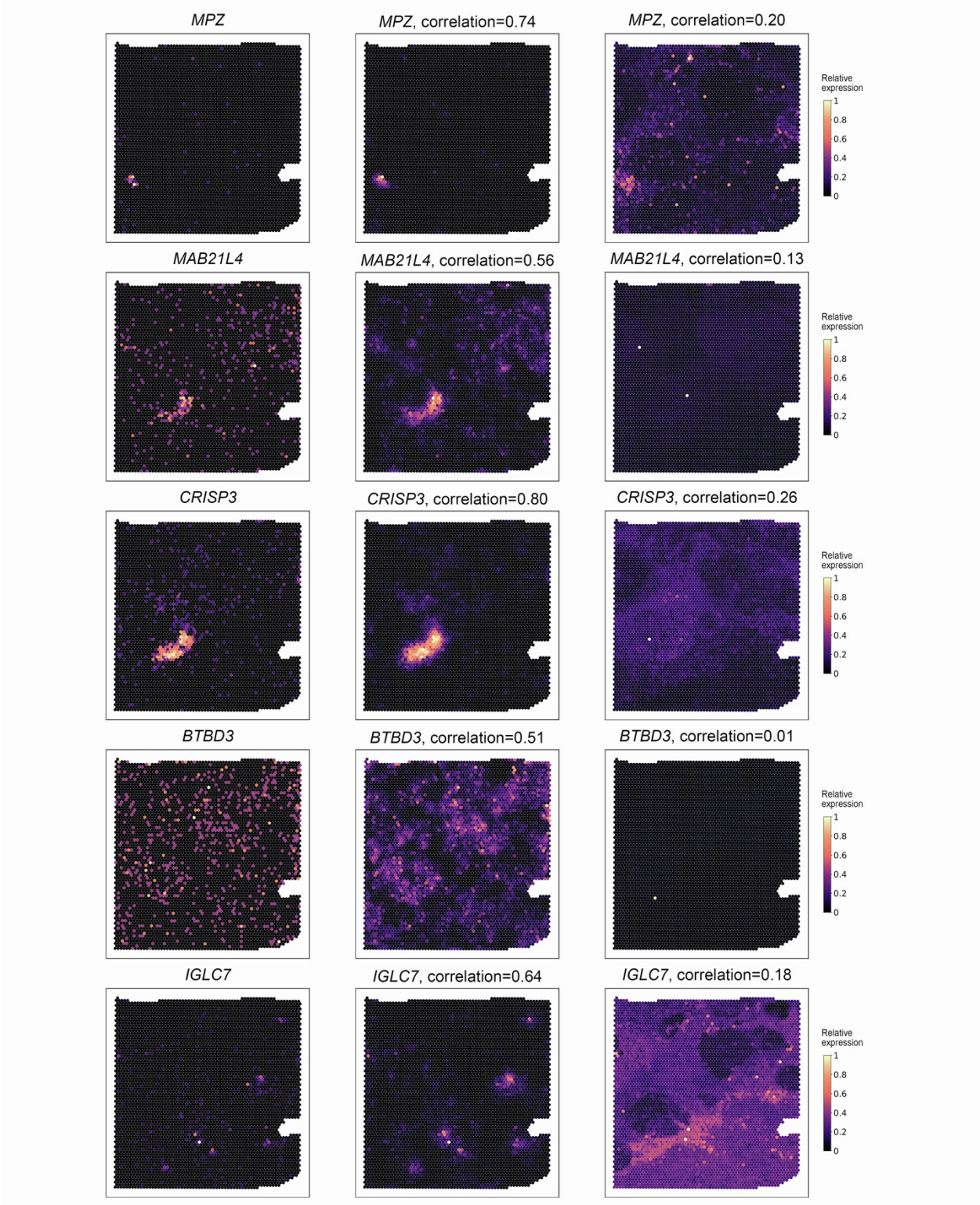
MPZ
MPZ, correlation=0.74
MPZ, correlation=0.20
MAB21L4
MAB21L4, correlation=0.56
MAB21L4, correlation=0.13
CRISP3
CRISP3, correlation=0.80
CRISP3, correlation=0.26
BTBD3
BTBD3, correlation=0.51
BTBD3, correlation=0.01
IGLC7
IGLC7, correlation=0.64
IGLC7, correlation=0.18
Relative expression
1
0.8
0.6
0.4
0.2
0

Fig. S2. Boxplot of number of cells in the pseudo Visium spots generated using the Xenium data. Each point in the boxplot represents a pseudo spot. The median equals 7 (n=3847). The lower and upper hinges correspond to the first and third quartiles, and the center refers to the median value. The upper (lower) whiskers extend from the hinge to the largest (smallest) value no further (at most) than 1.5 × interquartile range from the hinge. Data beyond the end of the whiskers are plotted individually.

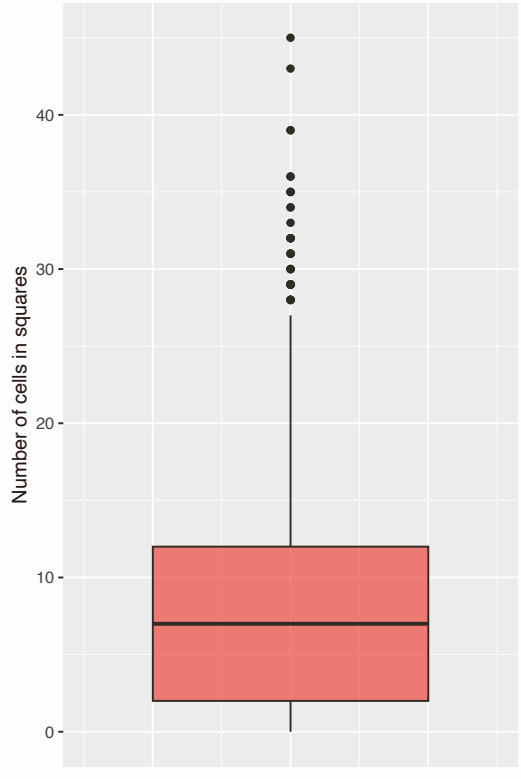

Fig. S3. Tumor marker gene images for the cutaneous squamous cell carcinoma tissue section generated by TESLA.

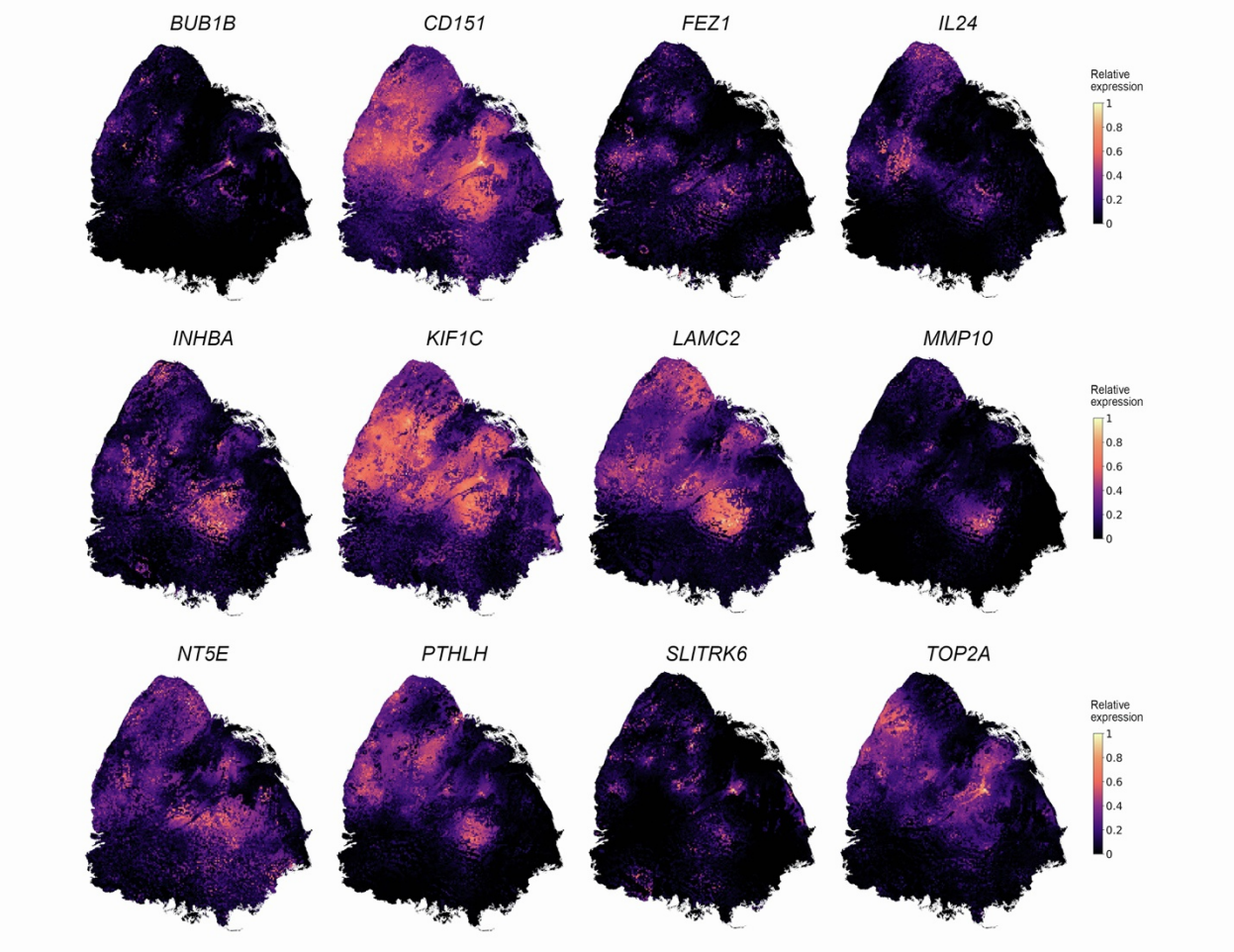

Fig. S4. Total UMI counts for the cutaneous squamous cell carcinoma tissue section.

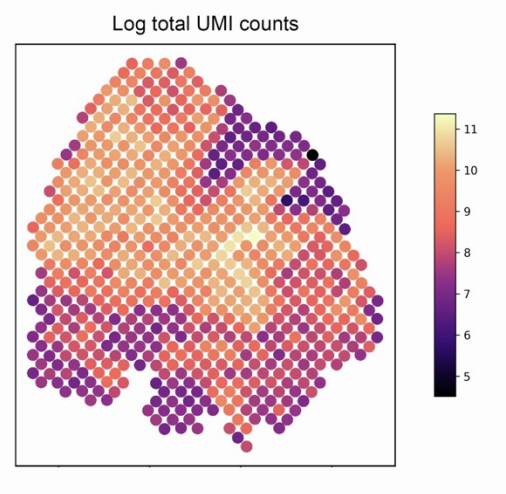

Fig. S5. Examples of TESLA identified genes that are highly enriched in the tumor core or edge in the human cutaneous squamous cell carcinoma dataset of the skin.

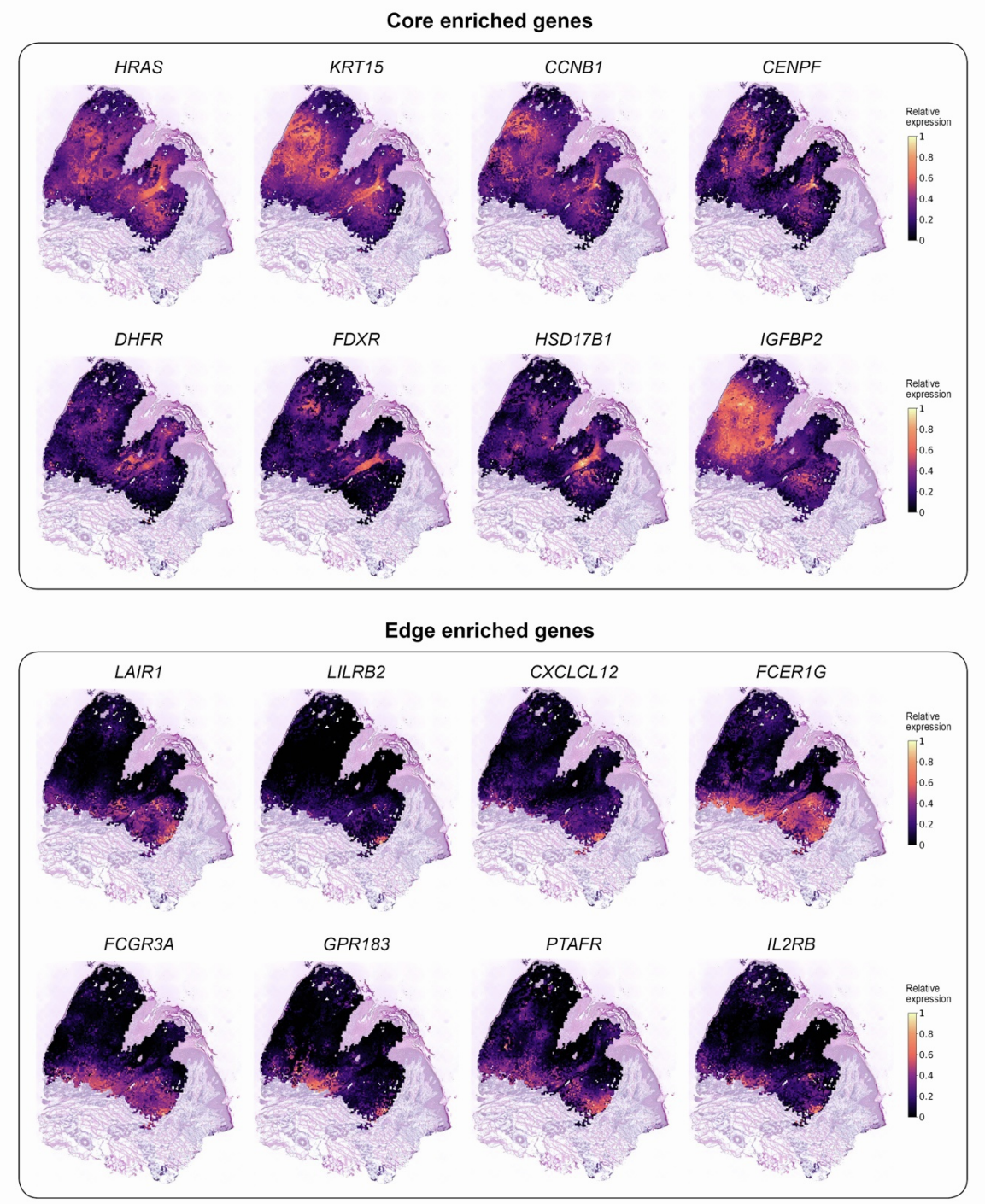

Fig. S6. Marker gene images for clinical melanoma diagnosis for the cutaneous malignant melanoma tissue section.

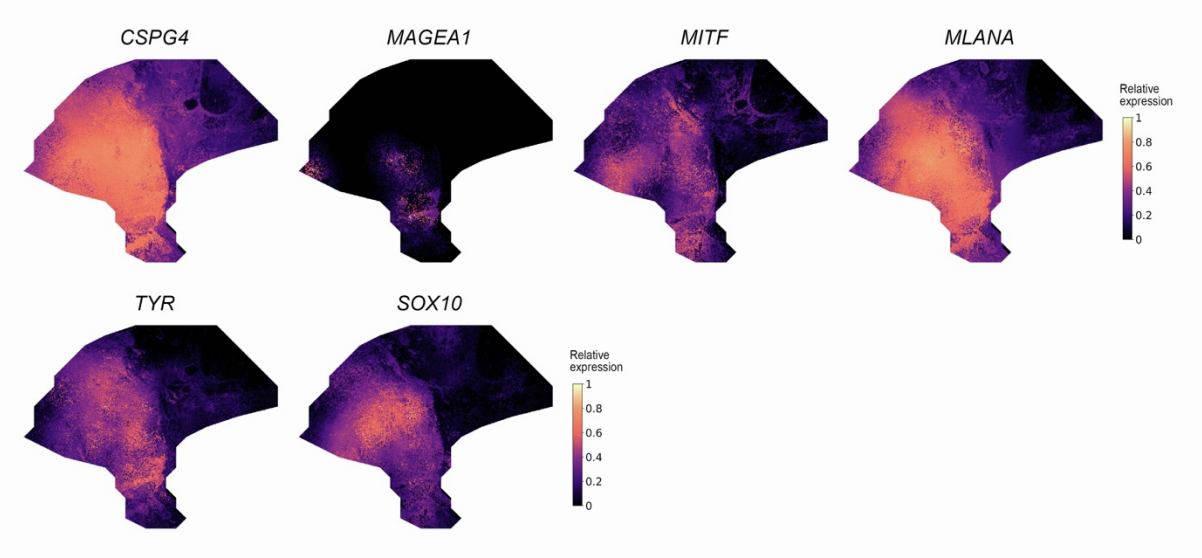

Fig. S7. Examples of TESLA identified genes that are highly enriched in the tumor core or edge in the human cutaneous malignant melanoma dataset.

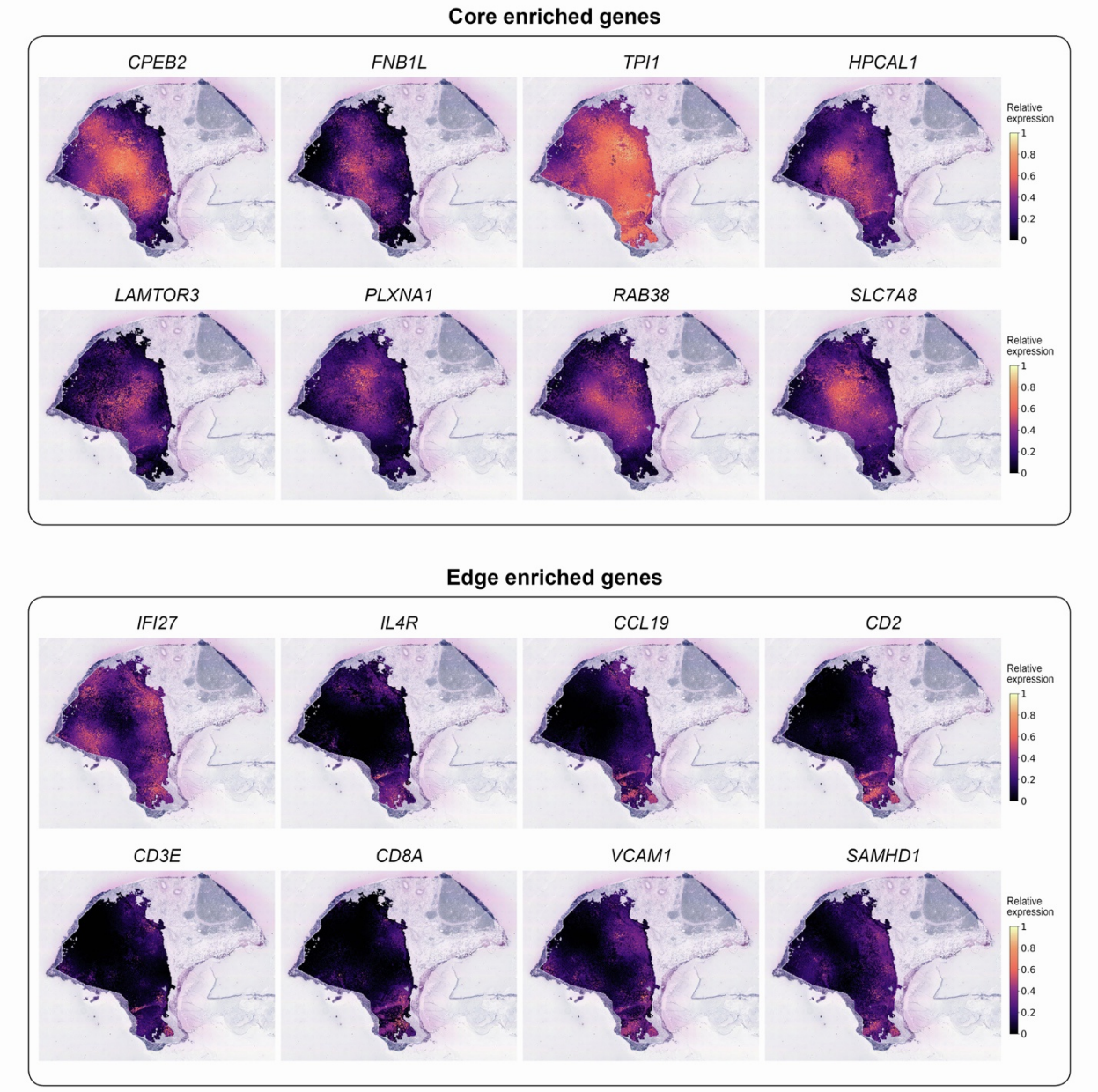

Fig. S8. Cell type distributions in tumor edge and core based on deconvolution results obtained from RCTD. CAF stands for cancer associated fibroblast.

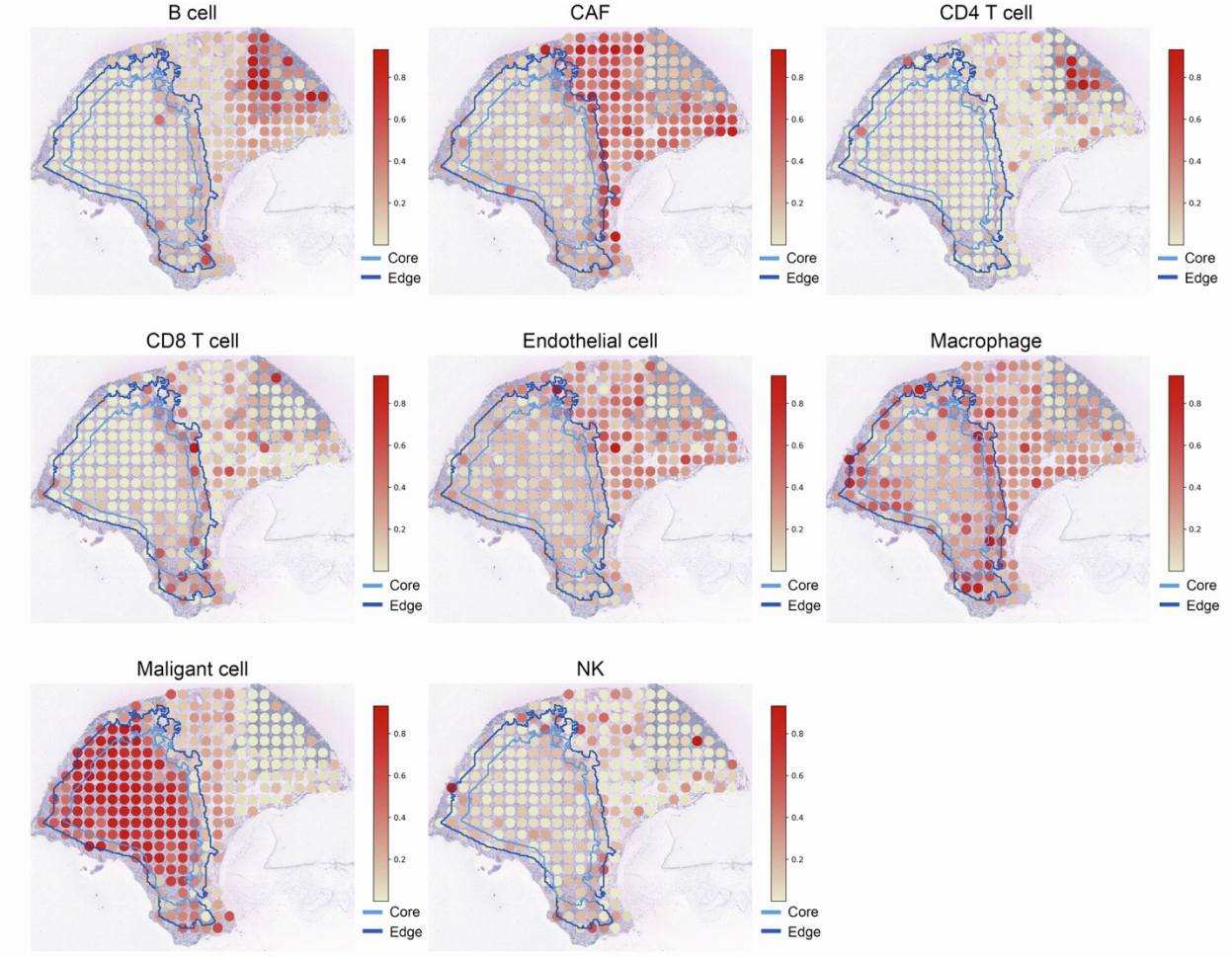

Fig. S9. Marker gene images for B cells, CD4+ T cells, dendritic cells, and CXCL13 in the squamous cell skin carcinoma dataset.

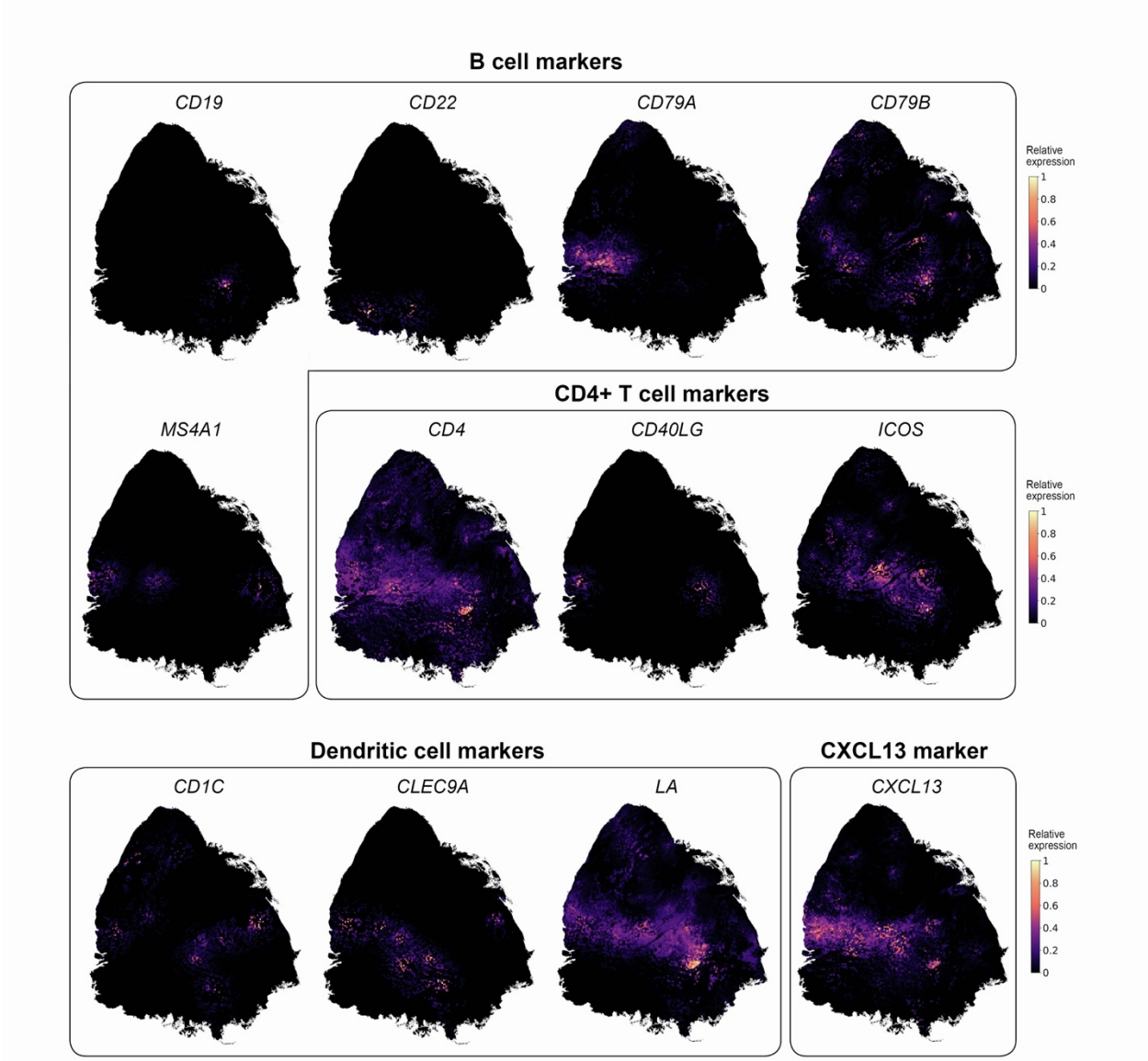

Fig. S10. Marker gene images for B cells, CD4+ T cells, dendritic cells, CD8+ T cells, and CXCL13 in the human cutaneous malignant melanoma dataset.

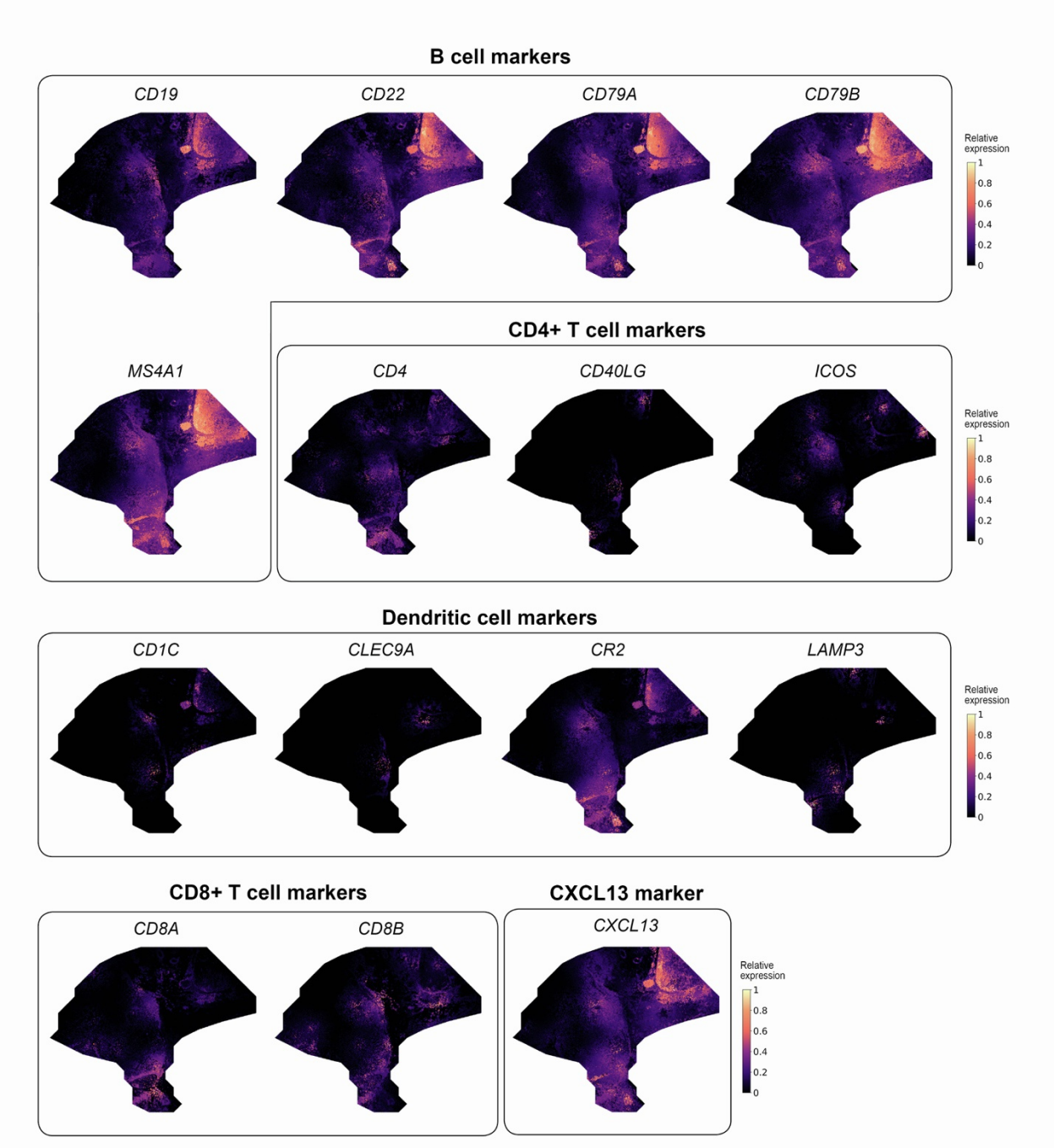

Fig. S11. Cell type deconvolution results for the CSCC data using RCTD.

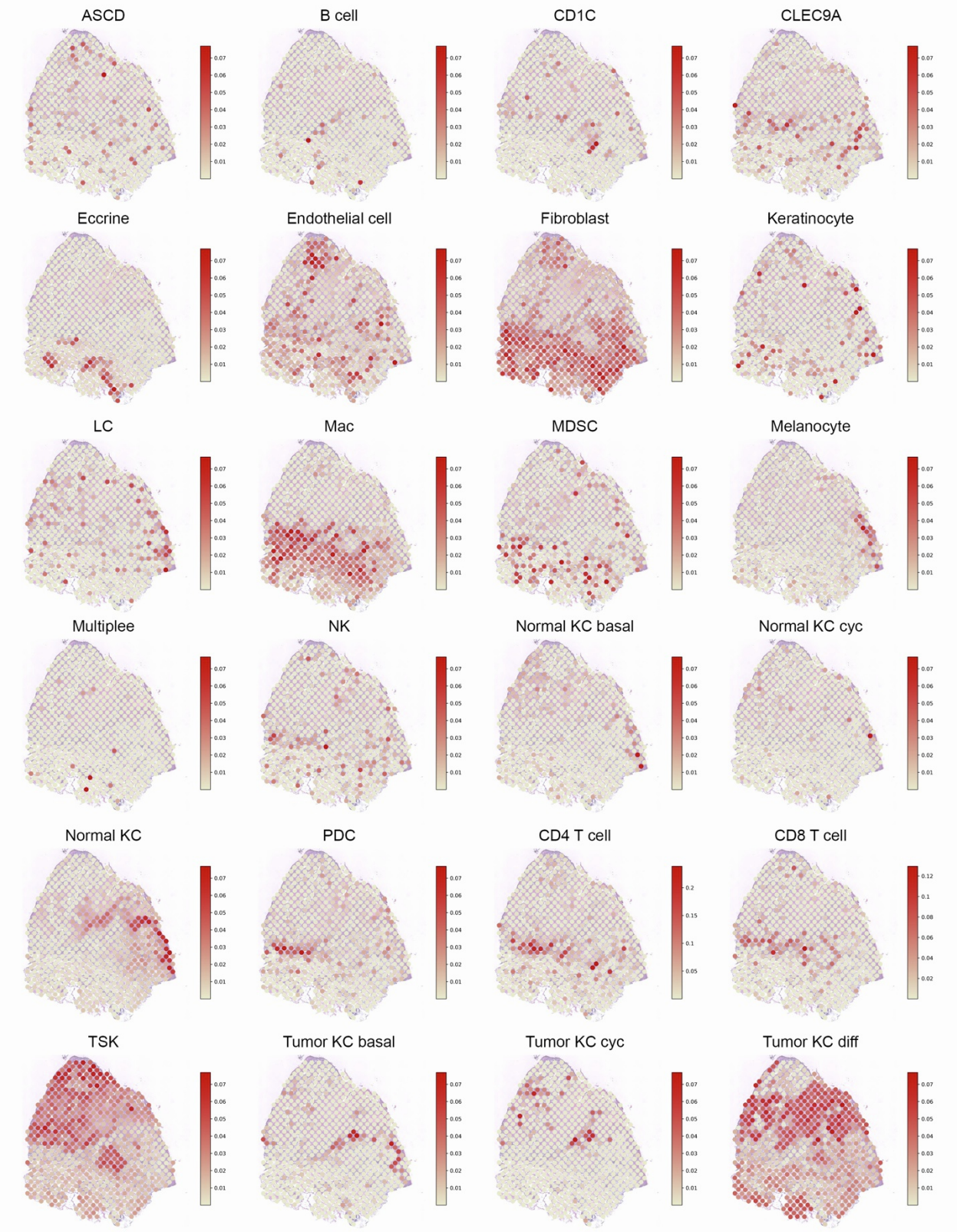

Fig. S12. Cell type deconvolution results for the human cutaneous malignant melanoma data using RCTD.

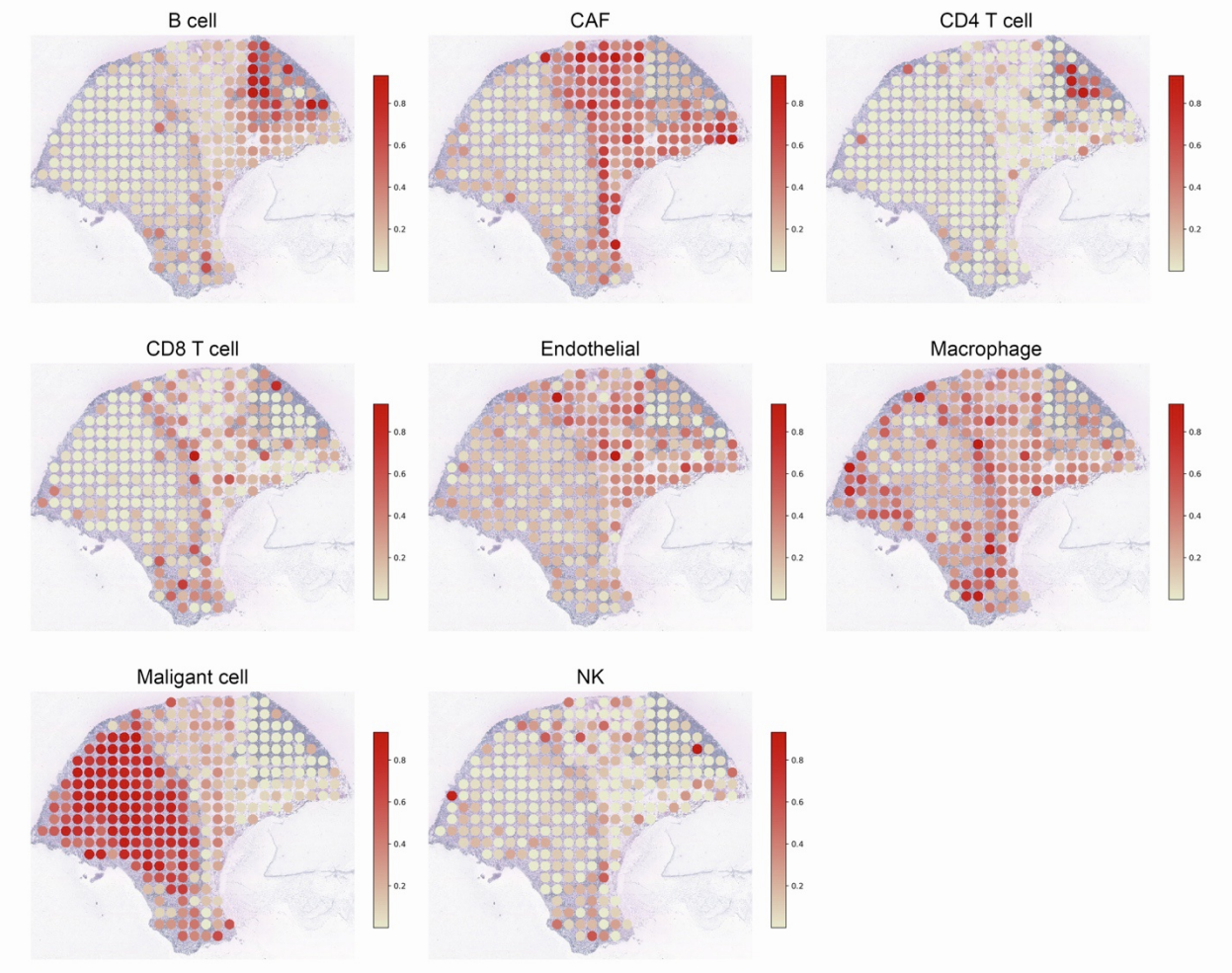

Fig. S13. Distribution of follicular helper T cells in the CSCC and Melanoma data from TESLA, using markers *CD3E, CD3D, CD3G, CD4, PDCD1, CXCR5*.

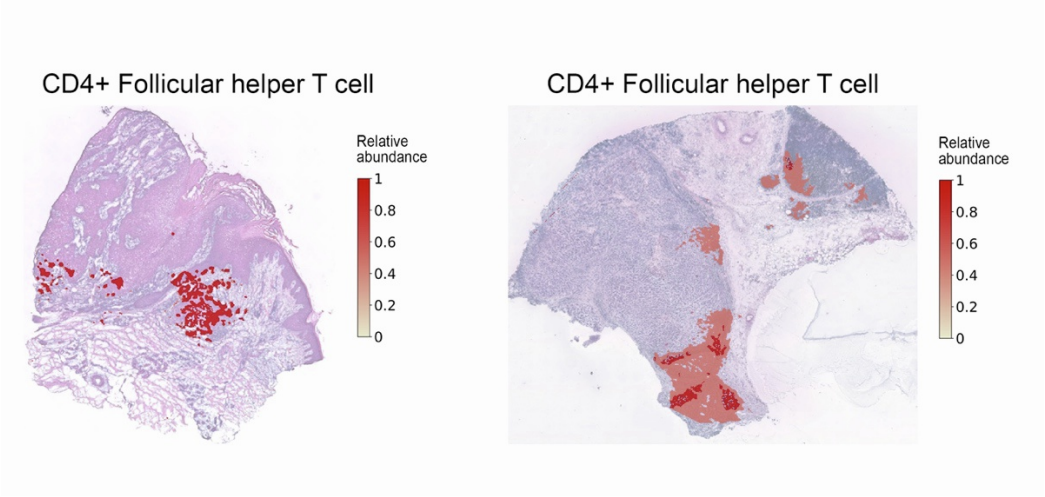

Fig. S14. Tumor marker gene images in the human breast cancer datasets.

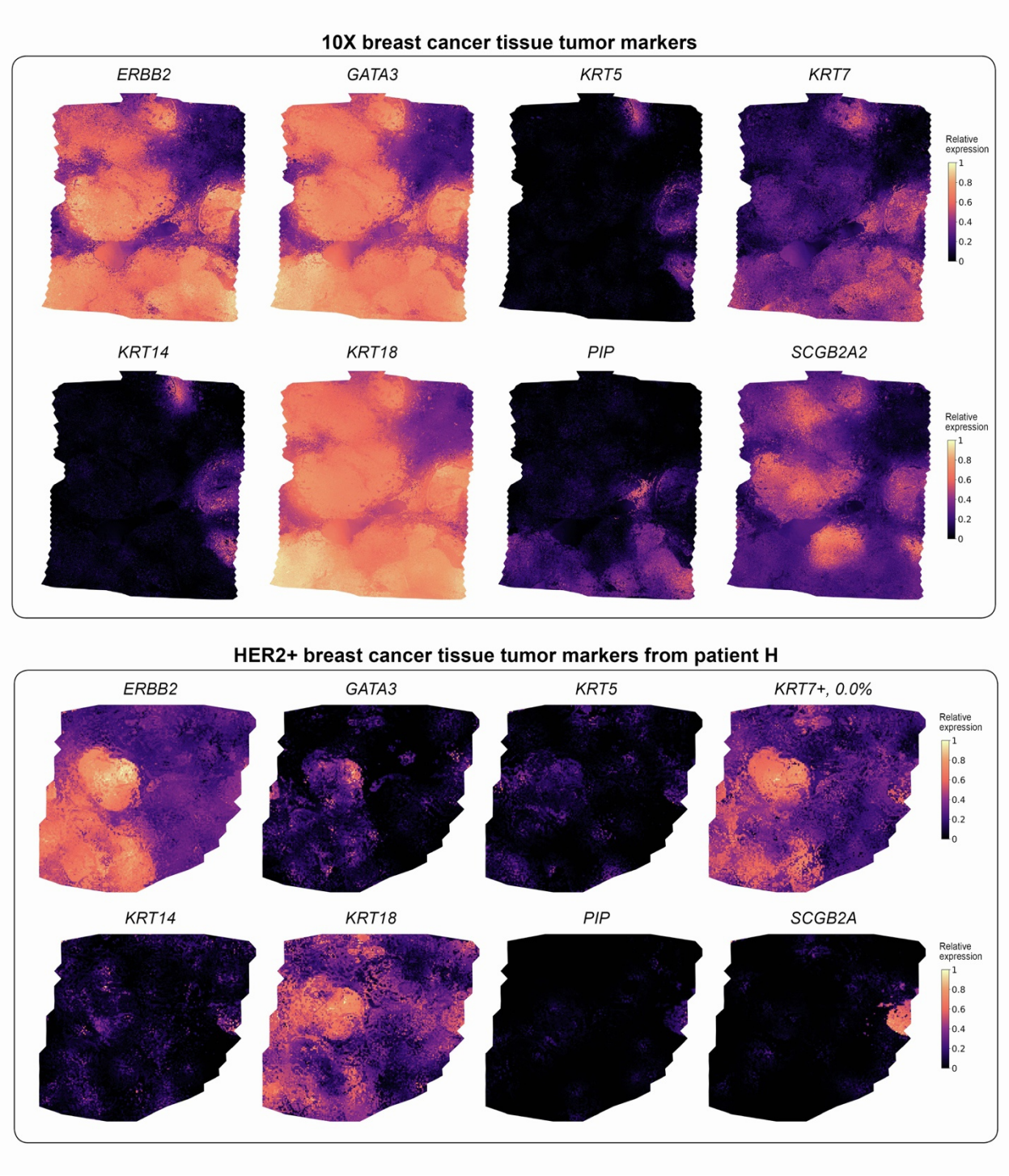

HER2+ breast cancer tissue tumor markers from patient G

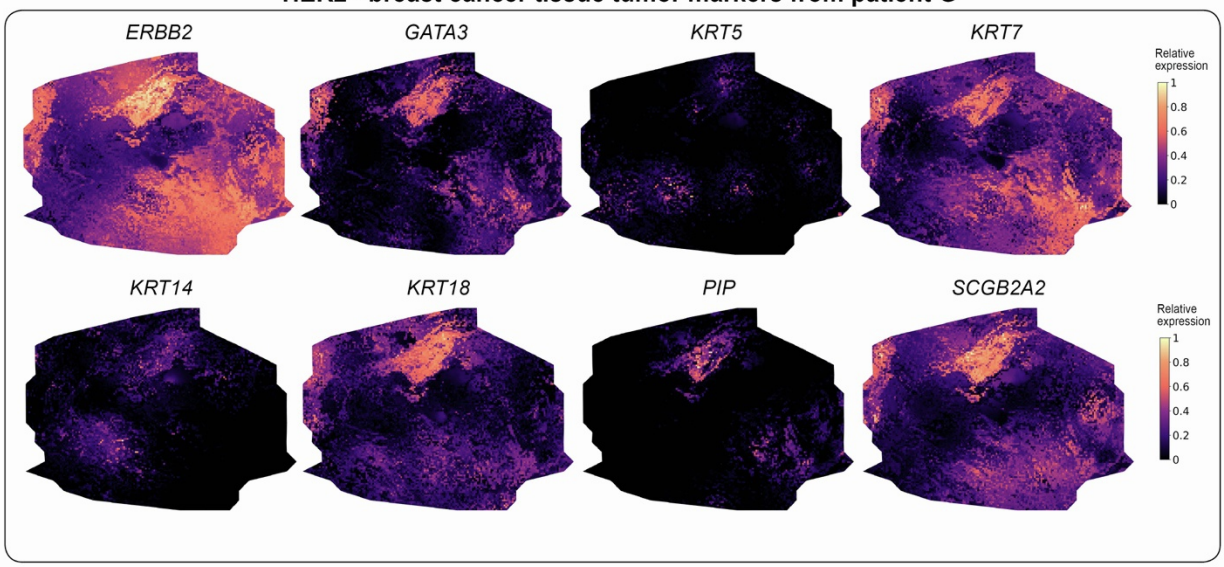

HER2+ breast cancer tissue tumor markers from patient B

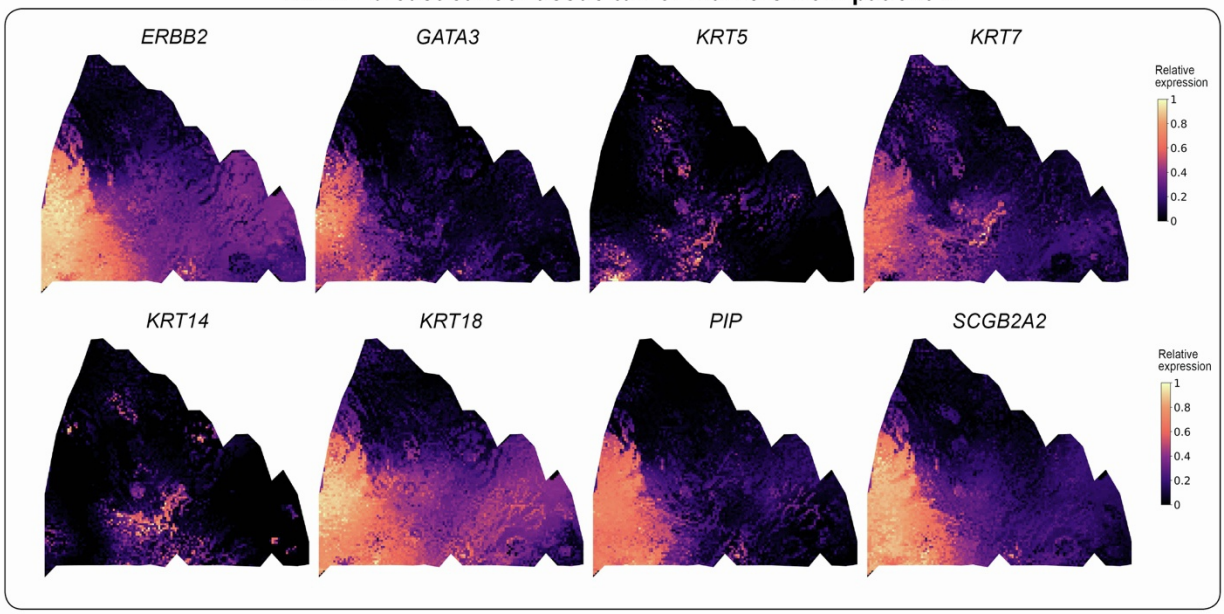

Fig. S15. Super-resolution meta gene from TESLA is able to correct artifact in protein immunofluorescence staining image.

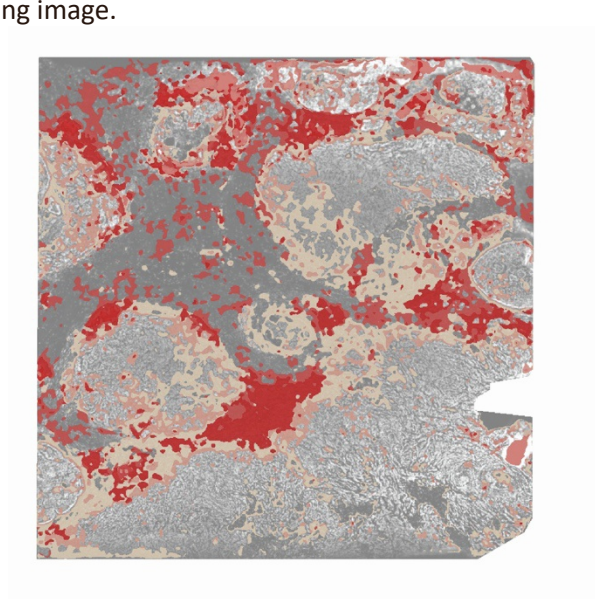

Note S1. Tissue coverage rate of different ST technologies.

For each dataset, we separated the whole tissue area into same sized grids where each grid unit contains the same number of spots with the same pattern as shown in **Fig. S16**. We then calculated the theoritical coverage rate using the area of spots inside the grid unit divided by the area of the grid. For 10x Visium, there are two spot layouts (10x Visium type1: invasive ductal carcinoma data; 10x Visium type2: squamous cell skin cancer cacinoma data), whose theoritical coverage rates are 25.6% and 45.8%, respectively, while for Spatial Transcriptomics (melanoma data; HER2+ breast cancer data), it has a theoritical coverage rate of 34.9%.

Additionally, we calculated the exact coverage rate for each analyzed dataset. We first detected the whole tissue region and calculated its area. Next, we derived the covered tissue area by multiplying the number of measured spots and the unit spot area. The coverage rate is computed as the ratio of covered tissue area to the whole tissue area. The invasive ductal carcinoma data from 10x Visium with pattern 1 has a coverage rate of 27.2% while the squamous cell skin cancer carcinoma data from 10x Visium with pattern 2 has a coverage rate of 48.5%. The melanoma and HER2+ breast cancer data from Spatial Transcriptomics have coverage rates of 21.4%, 20.4% (patient B), 20.3% (patient G), and 20.4% (patient H), respectively.

Fig. S16. Spot layout in different ST technologies.

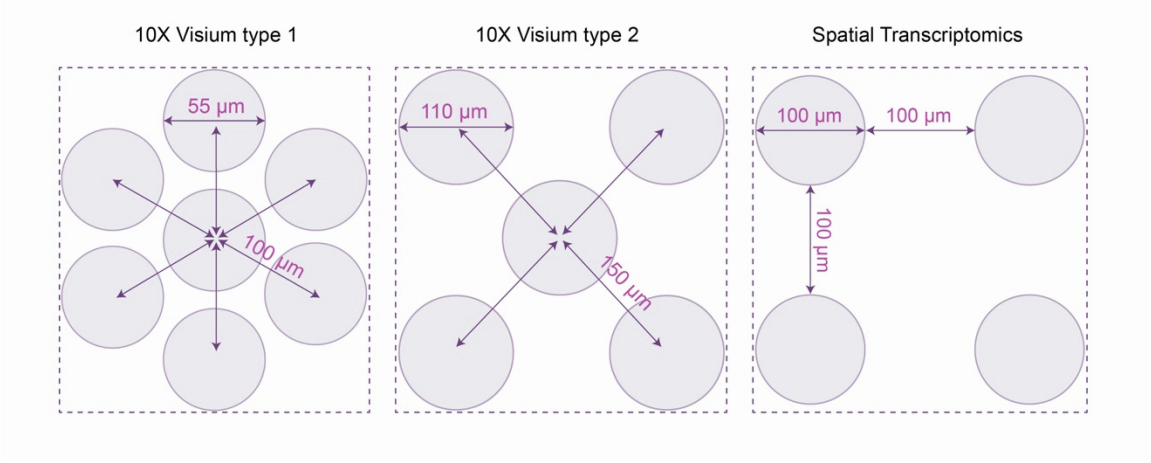

Note S2. TESLA's gene expression enhancement will not blur the tumor boundary.

We provide some examples to show how the original gene expression and H&E image affect the region boundary in TESLA's enhanced gene expression. As shown in **Fig. S17**, in the melanoma dataset, the tumor (left), normal (middle), and lymphoid aggregate (upper-right) have very different morphology features in the H&E image. MIFT is a marker gene for tumor, and after TESLA's enhancement, the tumor-normal boundary is still clear. Similarly, CD19 is a marker gene for B cells, and its enhanced gene expression still reveals the detailed structure of the lymphoid aggregate. An opposite example is PMEL, which is also a marker gene for tumor. However, this gene has blurred normal-tumor boundary after TESLA's enhancement. By checking the original spot-level data, we found that the boundary in the original data is not as clear as MITF, which led to the blurred boundary after enhancement. Based on these results, we think TESLA will not blur tissue boundaries or add artificial boundaries that are not present in the original gene expression.

Fig. S17. H&E, original and TESLA enhanced gene expression of MITF, CD19 and PMEL for the human cutaneous malignant melanoma data.

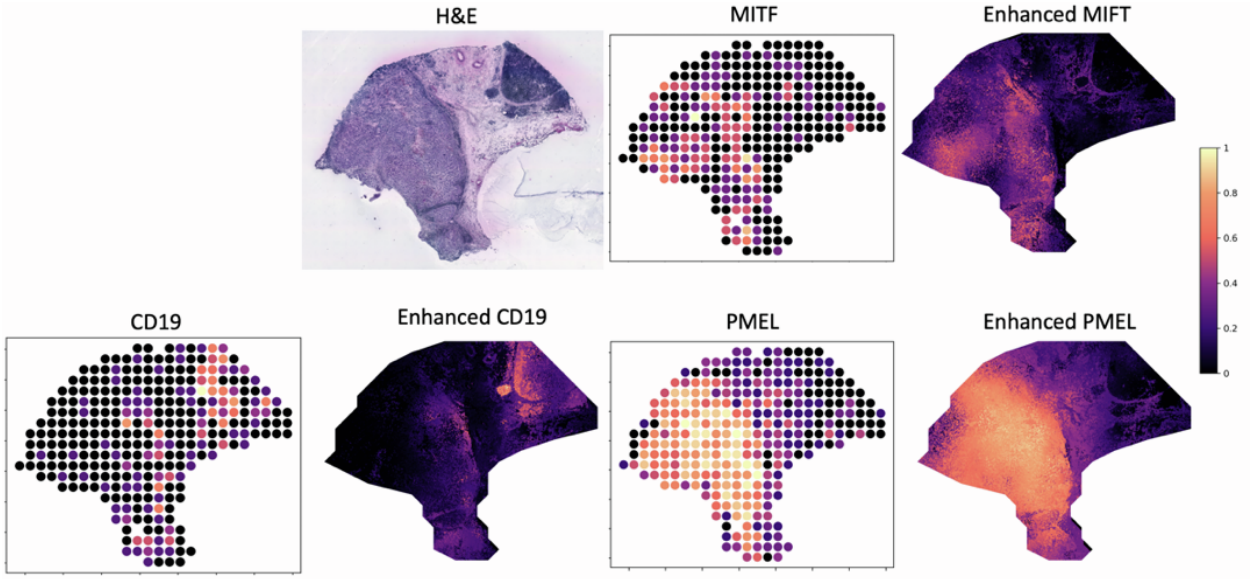

Note S3. Comparison of TESLA with XFuse using the CSCC data.

We compared TESLA with XFuse using the CSCC data in two aspects: 1)Run time: The gene expression enhancement step in TESLA only took less than 5 minutes on a CPU machine, while it took XFuse 17 days (408.5 hours) on the same machine. 2)The Pearson correlation between the original spot level and the enhanced gene expression for tissue region that overlaps with spots. This comparison is to ensure that the enhanced gene expression retains the original expression pattern and does not generate artificial patterns. XFuse automatically filtered out 7376 genes. Among the remaining 9968 genes that it predicted, we selected the top 2000 highly expressed genes for evaluation. We calculated the Pearson correlation between the spot-level enhanced gene expression and the original gene expression for TESLA and XFuse. As shown in **Fig. S18**, the median Pearson correlation for TESLA is 0.74 while the median Pearson correlation for XFuse is only 0.20. As admitted by the XFuse authors, their method may perform well only for a limited number of genes. This is not surprising as XFuse's performance is highly dependent on the histology image. For genes whose expression patterns are not similar to histology image, XFuse does not perform well. Given how slow XFuse is, its lack of flexibility in generating super-resolution gene expression in a transparent manner, and its poor performance in our evaluations, we think it is not necessary to run XFuse for the remaining datasets included in this paper.

Fig. S18. Boxplot of Pearson correlations between the original spot-level gene expression and "spot-level" gene expression obtained from the enhanced expression generated from TESLA and XFuse for the top 2,000 highly variable genes (n=2000). The lower and upper hinges correspond to the first and third quartiles, and the center refers to the median value. The upper (lower) whiskers extend from the hinge to the largest (smallest) value no further (at most) than 1.5 × interquartile range from the hinge. Data beyond the end of the whiskers are plotted individually

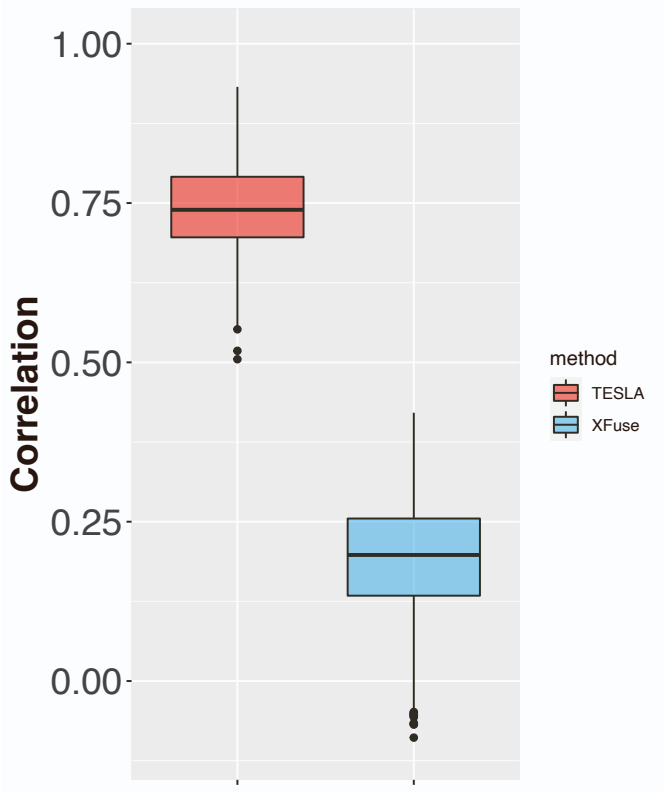

Note S4. The cellular and molecular spatial structure of tumor cannot be revealed with original spot-level data.

To showcase the strength and necessity of TESLA's super-resolution annotation, we analyzed the CSCC and melanoma datasets using their original spot-level data and compared with results obtained from TESLA. We first performed spatial clustering analysis using SpaGCN, a spatial clustering method that we previously developed for spatial domain detection in spatial transcriptomics. SpaGCN operates at the spot-level. We performed spatial clustering analysis with different resolution parameter values, leading to different number of clusters, i.e., spatial domains. As shown in **Fig. S19** and **S20**, using spot-level gene expression data as input, clustering analysis cannot identify spatial domains that capture the tumor edge and core structure for both datasets, regardless how many clusters were specified in the clustering analysis.

Next, we show that the edge and core enriched genes can only be detected at the super-resolution level. To demonstrate this point, we first assigned the identity of each spot based on the tumor edge and core separation obtained from TESLA for both CSCC and cutaneous malignant melanoma data (**Figure S21 a,b**). Then, we performed core vs edge differential expression (DE) analysis at the spot level using the same filtering criteria as we did for the super-resolution gene expression data.

For the CSCC, we detected 3,665 genes enriched in tumor core and 106 genes enriched in tumor edge when using the super-resolution gene expression data as input, but when using the spot-level gene expression data as input, we only detected 1,023 enriched genes for the tumor core (765 genes overlap with super-resolution detection) and 0 enriched genes for the tumor edge. Similarly, for the melanoma dataset, we detected 3,510 genes enriched in tumor core and 155 genes enriched in tumor edge when using super-resolution gene expression data as input for DE analysis. But when using the spot-level gene expression as input, we only detected 1,632 genes enriched for the core (1509 genes overlap with super-resolution detection) and 1 gene ("BGN") enriched for the edge (1 gene overlaps with super-resolution detection).

The above results show that the super-resolution gene expression data are needed to identify tumor core and tumor edge enriched genes, especially for the tumor edge. We think the failure of detecting tumor edge enriched genes at the spot level is due to two reasons. First, the number of observations is much smaller when considering spot as the analysis unit, and the reduced sample size in DE analysis will lead to less power. Second, the spot-level data do not have single-cell resolution. Indeed, the diameter size of each spot is 100um in Spatial Transcriptomics, which is much larger than a single cell. Since each spot may contain many cells, the mixture of cells from different cell types will dilute the differential expression signal, especially when the immune cells are rare. Therefore, we believe that until the sequencing-based spatial transcriptomics technologies reach to single-cell resolution, gene expression resolution enhancement will be needed when the goal is to detect gene expression changes that occur only in a small region of the tissue.

Fig. S19. Spatial domains detected using SpaGCN with different numbers of domains for the CSCC data.

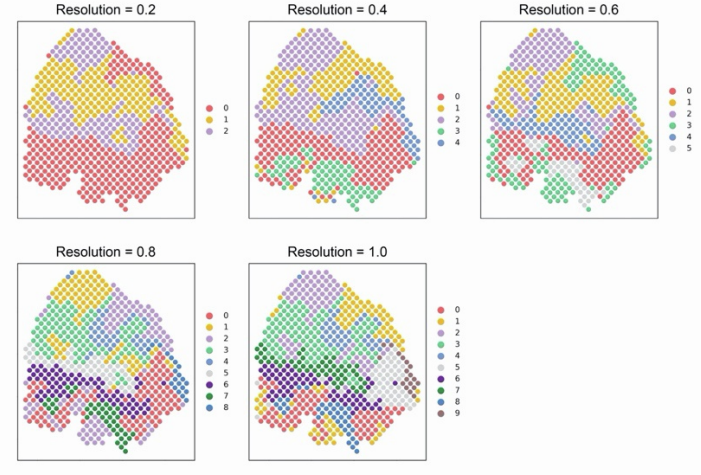

Fig. S20. Spatial domains detected using SpaGCN with different numbers of domains for the melanoma data.

Fig. S21. Spatial domains detected using SpaGCN with different numbers of domains for the melanoma data.

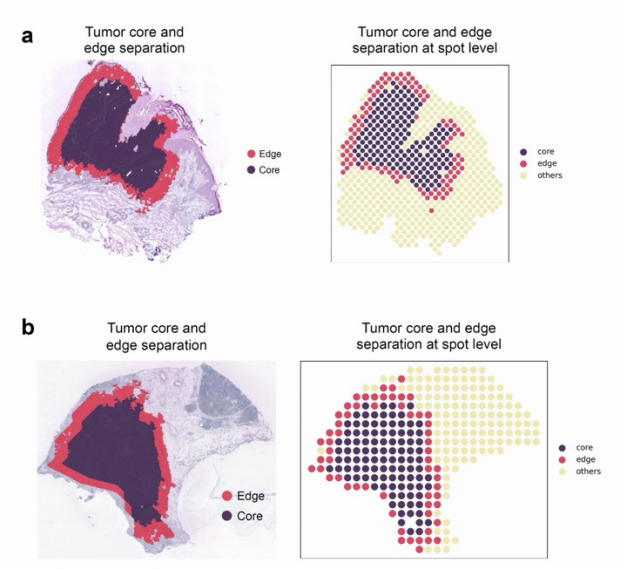

Supplementary Note S5. Annotation of mouse posterior brain using TESLA.

TESLA is a generic framework and can be applied to any tissue as long as high-resolution histology images are available. To show the flexibility of our method, we performed spatial domain annotation for a 10X Visium mouse brain dataset using TESLA. We picked Spatially Variable Genes (SVGs) for different brain regions reported in our previous publication SpaGCN [1]. Next, we used these SVGs to identify brain regions at super-resolution using TESLA. As shown in **Fig. S22**, TESLA can successfully identify distinct neuroanatomic subregions in the brain with "granular cell layer of the cerebellum" shown on the left and "molecular layer of the cerebellum" shown on the right. The clear boundaries between these two neuroanatomic subregions indicate the high accuracy of TESLA in spatial domain annotation in non-cancer tissues.

Fig. S22. Distinct neuroanatomic subregions, granular cell layer of the cerebellum (left) and molecular layer of the cerebellum(right), detected by TESLA.

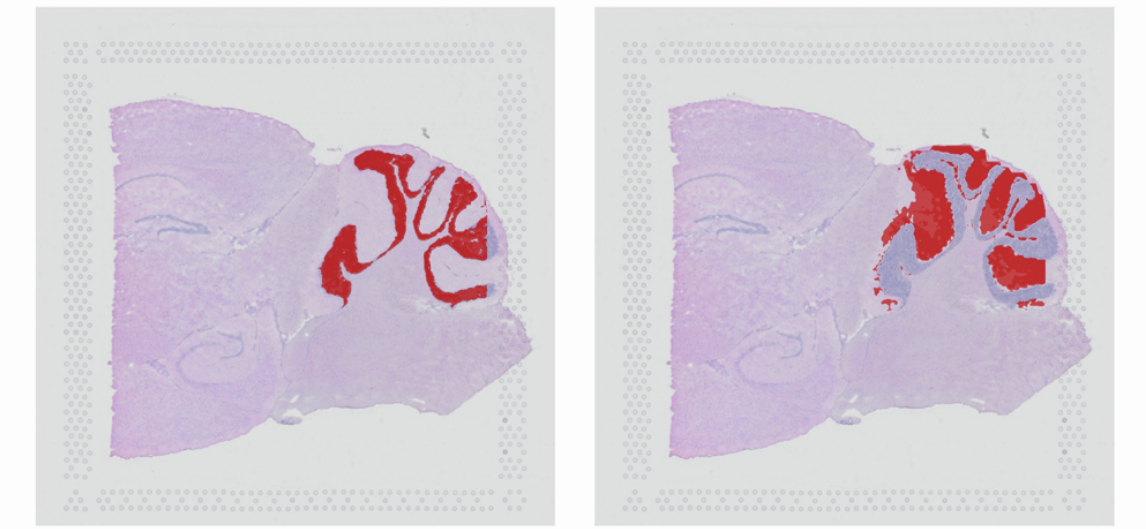

Note S6. Computation cost of TESLA, BayesSpace on the IDC dataset.

TESLA is computationally fast and memory efficient. To showcase the computational advantage of TESLA, we recorded its run time and memory usage for the IDC data and compared with BayesSpace. All analyses were conducted on Mac OS 10.13.6 with single Intel® Core(TM) i5-8259U CPU @2.30GHz and 16GB memory. As shown in **Fig. S23**, TESLA completed gene expression enhancement in 19 minutes, whereas the computing time was more than 11 hours for BayesSpace. Furthermore, TESLA only required 10.0GB of memory, whereas BayesSpace required 12.9 GB of memory.

Fig. S23. TESLA and BayesSpace time and memory usage comparison using the IDC dataset.